Diamine Surface Passivation and Post-Annealing Enhance Performance of Silicon-Perovskite Tandem Solar Cells

Margherita Taddei,[1] Hannah Contreras,[1] Hai-Nam Doan,[2,3] Declan P. McCarthy,[4] Seongrok Seo,[2] Robert J. E. Westbrook,[1] Daniel J. Graham,[5] Kunal Datta,[6] Perrine Carroy,[7] Delfina Muñoz,[7] Juan-Pablo Correa-Baena,[6] Stephen Barlow,[8] Seth R. Marder,[4,9,8] Joel A. Smith,[2] Henry J. Snaith,[2] David S. Ginger[1,10]*

1 Department of Chemistry, University of Washington, Seattle, WA 98195, USA

2 Department of Physics, University of Oxford, Oxford, OX1 3PU, U.K.

3 Institute of Materials Science, Technical University of Munich, München, 85748, Germany

4 Department of Chemistry, University of Colorado-Boulder, Boulder, CO 80309, USA

5 Department of Bioengineering, University of Washington, Seattle, Washington 98195

6 School of Materials Science and Engineering, Georgia Institute of Technology, North Ave NW, Atlanta, Georgia 30332, USA

7 Université Grenoble Alpes, CEA, Liten, Campus Ines, 73375 Le Bourget du Lac, France

8 Renewable and Sustainable Energy Institute, University of Colorado-Boulder, Boulder, CO 80309, USA

9 Department of Chemical and Biological Engineering and Materials Science Program, University of Colorado-Boulder, Boulder, CO 80309, USA

10 Physical Sciences Division, Physical and Computational Sciences Directorate, Pacific Northwest National Laboratory, Richland, Washington 99352, United States

* Corresponding author, email: dginger@uw.edu

Abstract:

We show that the use of 1,3-diaminopropane (DAP) as a chemical modifier at the perovskite/electron-transport layer (ETL) interface enhances the power conversion efficiency (PCE) of 1.7 eV bandgap FACs mixed-halide perovskite single-junction cells, primarily by boosting the open-circuit voltage (V_{OC}) from 1.06 V to 1.15 V. We find that adding a post-processing annealing step after C60 evaporation further improves device performance. Specifically, the fill factor (FF) increases by 20% in the DAP + post-annealing devices compared to the control. Using hyperspectral photoluminescence microscopy, we demonstrate that annealing helps improve compositional homogeneity at the electron transport layer (ETL) and hole transport layer (HTL) interfaces of the solar cell, which prevents detrimental bandgap pinning in the devices and improves C_{60} adhesion. Using time-of-flight secondary ion mass spectrometry, we show that DAP reacts with formamidinium (FA^+) present at the surface of the perovskite lattice to form a larger molecular cation, 1,4,5,6-tetrahydropyrimidinium (THP^+) that remains at the interface. Combining the use of DAP and annealing the C_{60} interface, we fabricate Si-perovskite tandems with PCE of 25.29%, compared to 23.26% for control devices. Our study underscores the critical role of the chemical reactivity of diamines at the surface and thermal post-processing of the C_{60}/Lewis-base passivator interface in minimizing device losses and advancing solar-cell performance of wide-bandgap mixed-cation mixed-halide perovskite for tandem application.

Keywords: perovskite; solar cell, Si-perovskite tandem; passivation; diamine

TOC:

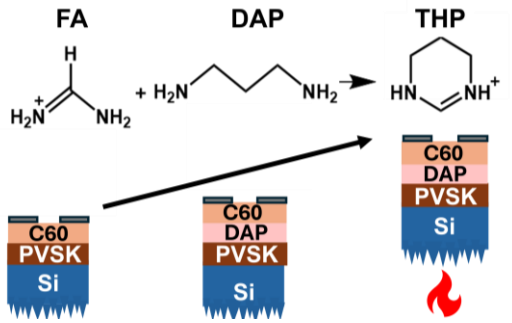

Introduction

A tandem solar cell is composed of a narrow band-gap bottom cell and wider band gap top cell.[1,2] This design can surpass the power conversion efficiency (PCE) of a single junction by more efficiently harvesting different regions of the solar spectrum, reducing charge carrier thermalization losses to produce cells with higher voltages. Silicon cells, with a bandgap of ~1.1 eV, can be used as the bottom cell and metal halide perovskites can be suitable active layers for the top cell, with an ideal bandgap of ~1.7 eV for the perovskite.[3–5] The development of Si-perovskite tandem solar cells has gained significant attention, with a record-breaking PCE of 33.9% achieved in 2023,[6] which exceeds the single-junction limit for a Si cell, but is still below that theoretical >43% radiative efficiency limit of an ideal Si-perovskite tandem.[1,6] Challenges persist, particularly regarding the development of perovskite top cells with band gaps above 1.7 eV. The mixed bromide-iodide compositions generally used for 1.7 eV perovskites often exhibit undesirable photoinduced phase segregation,[7,8] leading to lower band-gap domains in which charges are "funneled",[9–11] decreasing the open-circuit voltage (V_{OC}) of the solar cell.[12–14] Furthermore, issues arise at the interface between the perovskite absorber and the charge-transporting layers, especially in such wide band-gap perovskite cells. Their deeper valence band maxima (VBM) and shallower conduction band minima (CBM) compared to more typical ~1.6 eV bandgap perovskite compositions result in unfavorable energetic offsets between the perovskite band edges and the transport levels of commonly used electron- (ETL) and hole-transport layers

(HTL).[15,16] Fullerenes have been widely used as electron-transport layers (ETLs) in p-i-n perovskite solar cells due to their suitable energy alignment, typically high electron mobility, and ease of processing in vertical device stacks.[17] However, the interface between perovskite and fullerenes is a primary source of efficiency loss in devices.[18–20] This loss primarily stems from charge recombination, particularly the recombination of electrons extracted to the fullerene layer with holes at the perovskite surface.[18,21] The process of charge trapping at the perovskite/ETL interface is also associated with the presence of current-voltage hysteresis in perovskite devices, by which differences are observed in the J-V curves measured in forward and reverse scan directions.[22] Shao and co-workers have shown that adding a layer of the C_{60}-derivative [6,6]-phenyl-C_{61}-butyric acid methyl ester (PCBM) between the perovskite and C_{60}, followed by an annealing step, resulted in hysteresis-free J-V curves.[23] They attributed the lack of hysteresis to PCBM filling grain boundaries of the perovskite layer after annealing, thus lowering the trap density at the perovskite/ETL interface. However, the use of PCBM is less desirable for future Si-perovskite tandem commercialization due to its sensitivity to light and air exposure, as well as stronger parasitic optical absorption and higher cost than for C_{60}.[24] Other perovskite/ETL interface passivation strategies have been implemented to mitigate interface recombination based on various Lewis base molecules.[25,26] The deposition of a Lewis base at the perovskite top surface can effectively enhance the photoluminescence quantum yield and reduce surface recombination velocity by passivating surface trap states in the perovskite,[27–29] and can reduce interfacial recombination of holes in the perovskite layer with electrons in the C_{60} layer by electronically decoupling the two layers.[30,31]

Amines have been shown to be a promising class of Lewis bases used to passivate bulk and surface defects in various perovskite compositions, both as additives and surface passivators.[10,32,33] The mechanism behind passivation though is still not as clear. A lot of work reports the use of

ammonium salts being used to fill A-site vacancies,[34] form lower dimensional phases,[35] or impart "field-effect passivation".[36–38] This term has been used to refer to ammonium ligands used to modify the surface potential of the perovskite layer and have a better energy alignment with the ETL to prevent interfacial recombination.[36] On the other hand, when using amines the mechanism of passivation has been often related to the formation of a coordinating bond between the metal in the B-site and the amine tail group,[39] and a similar chelating effect for diamines.[32,33] This passivation mechanism of coordinating Pb^{2+}/Sn^{2+} has been the most widely accepted. However, we have recently shown that when amines are used in formamidinium (FA^+) containing perovskite compositions, more chemical reactions need to be considered. In particular, we have demonstrated that a series of addition and elimination reactions can generate larger molecules when ethylenediamine (EDA) and benzylamine (BA) are introduced in the perovskite precursor.[10,40] In this work, we aim to verify whether the same chemical reaction between the amine ligand and FA^+ occurs when the amine is used solely as a surface passivator, rather than an additive. To this end, we investigate the combined effect of using an amine-based surface passivator, 1,3-diaminopropane (DAP), and post-processing annealing of C_{60} and a 1.7 eV mixed-cation mixed-halide perovskite in Si-perovskite tandem devices.

Results and Discussion

First, we fabricated single-junction p-i-n perovskite solar cell devices using Me-4PACz as a self-assembled monolayer (SAM) hole-transport layer (HTL) and deposited on a sparse alumina nanoparticles interlayer, which improves the wettability of the overlaying perovskite layer.[10,41] We use a mixed-cation mixed-halide perovskite composition $FA_{0.83}Cs_{0.17}Pb(I_{0.75}Br_{0.25})_3$ which has a bandgap of ~ 1.70 eV, ideal for Si-perovskite tandems.[10] We then spin coat a solution of 1,3-diaminopropane (DAP) in isopropanol with the optimized concentration of 0.75 mM on top of the perovskite. In **Figure S1** we show the device performance across a range of DAP concentrations,

revealing that optimal performance is achieved at concentrations between 0.75 and 1 mM. Following DAP deposition, we evaporate a layer of C_{60} (thickness of 30 nm) as the electron-transport layer (ETL) and bathocuproine (BCP, thickness of 8 nm) as a hole-blocking layer. We anneal for 1 minute at 150 °C after deposition of the ETL and BCP layers before depositing the silver top electrode. The 1-minute annealing step at 150 ºC is based on previous reports showing that this condition promotes covalent bonding between C60 and amine passivators such as polyallylamine.[42] The further control of the time and temperature dependence effect on the device performance of the post-annealing process is beyond the scope of this work and would be of great interest for future studies.

In **Figure 1a, b, c** and **d** we show the performance results of solar cells (active area 0.0453 cm^2) made without the DAP deposition step (denoted here after as "control"). The performance is improved when introducing the DAP surface passivator in the stack ("DAP") and annealing after C_{60} evaporation (denoted here after as "Control + annealing" and "DAP+ annealing"). The full devices architectures are shown in **Figure S2**. The maximum PCE recorded for the control device was 15.49% under forward scan which improved to 18.24% with DAP and further to 19.11% after DAP + annealing. The fill factor improved the most, increasing from 63.4% in the control and 73.3% with DAP, to values over 75% after annealing. In **Figure S3** we show that the annealing step also has a positive impact when using other amines, such as lysine and polyallylamine, as interlayers. However, we achieved the best results using DAP as the interlayer for this perovskite composition. The J-V curves of a typical device for each processing condition are shown in **Figure S4** and the mean and standard deviation values of devices of Figure 1 listed in **Table S1**. We monitored the stability of the control and DAP-treated devices by measuring the performance of encapsulated devices over a period of 324 hours in 1 Sun-equivalent constant illumination under open-circuit conditions at 85 °C (ISOS L-2).[43] In **Figure S5,** we show how the PCE, V_{OC}, FF and

J_{SC} varied over time over the course of the aging period. We find that devices subjected to the annealing step, both control and DAP-treated, exhibit improved retention of power conversion efficiency (PCE) after aging. We quantify it by calculating the percentage decrease of PCE between the first and last day of testing. Specifically, the PCE decreased by 92% and 83% for the control and DAP-treated devices, while the annealed counterparts showed a much smaller decrease of 67% (control + annealing) and 75% (DAP + annealing). The most striking difference is observed in the open-circuit voltage (V_{OC}). After 324 hours of aging, the V_{OC} dropped by only 9% for the control + annealing and 29% for the DAP + annealing device, compared to substantial decreases of 64% and 58% in the unannealed control and DAP-treated devices, respectively. The decrease in J_{SC} and FF are more comparable among the devices, with values varying between 60-35% from the initial one. The stability of the V_{OC} and steady improvement of the FF after aging suggests that the annealing is a promising step for improving device stability as well as performance. Moreover, we investigated whether the device performance increased with annealing prior to the evaporation of C_{60}. **Figure S6** shows the performance of control and DAP-treated devices that were either annealed before ("ANNEAL PVK") or after the evaporation of C60 and BCP ("ANNEAL C60"). The highest PCE was observed when using DAP combined with post-C60 annealing, confirming this as the most effective approach.

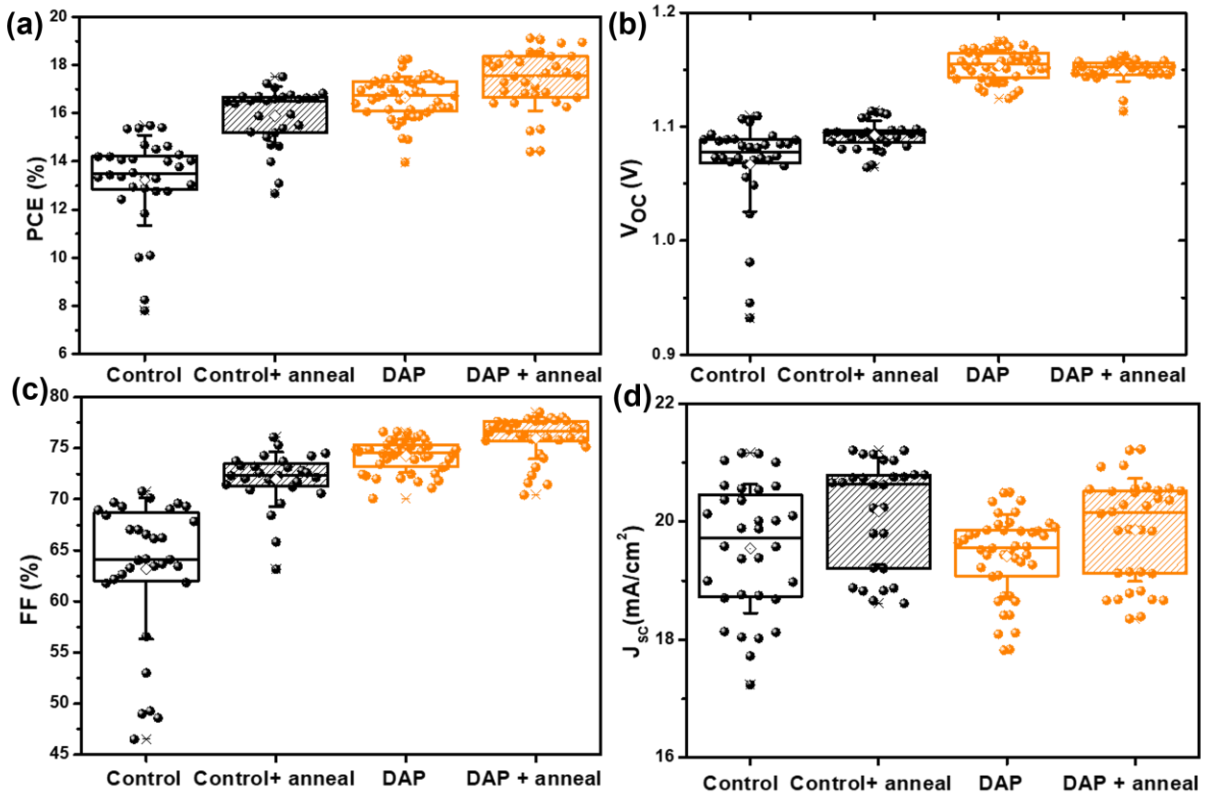

***Figure 1**: a) Power conversion efficiency (PCE) values, b) open-circuit voltage (V_{OC}), c) fill factor (FF) and d) short-circuit current density (Jsc) for the control device ("Control", black), DAP-treated ("DAP", orange) and Control and DAP-treated with a further annealing step at 150°C for 1 minute after C_{60} deposition ("Control + anneal", black, striped and "DAP + anneal", orange, striped).*

To better understand the impact on the FF, in **Figure S7** and **S8** we examine C_{60} coverage by recording photoluminescence (PL) maps of the devices. We see that the control device has more "bright spots" with higher PL and longer lifetime, which we attribute to the absence of C_{60}, and associated PL quenching (**Figure S9**). The devices treated with DAP and annealing have fewer bright spots, indicative of better C_{60} coverage. The reduced number of bright spots in DAP-treated and annealed samples suggests that the use of DAP and subsequent annealing of the C_{60} interface may reduce the number of pinholes in the ETL layers resulting in higher FF. To gain insights into

how the DAP deposition step and the annealing process affect the optoelectronic properties, we conducted hyperspectral PL microscopy on the full device stack (**Figure 2**). By using a hyperspectral microscope, we obtain a PL spectrum at every pixel with high spatial resolution. This technique has been used to spatially resolve heterogeneity in perovskites and other semiconductors.[10,44–47] Here, we capture hyperspectral images after excitation from the top surface of the perovskite, comparing the different treatments. We use a mercury halide lamp in the 350 – 450 nm range, which penetrated approximately 50 nm into the material, at 130 mW/cm^2 excitation intensity for ~5 minutes.[48]

We include the PL intensity maps in **Figure S10** and the average PL spectra in **Figure S11**, which show higher PL intensity for the DAP-treated full stack devices analyzed from the top interface compared with the untreated devices. In **Figure 2** we show the PL peak emission wavelength of the samples. The presence of "wrinkled" regions of redshifted and blueshifted PL has been previously shown for these wide gap mixed cation mixed halide compositons.[7,9,10,49,50] In **Figure S12a-d,** we show the PL peak wavelength map excited and collected from the top side Glass/BCP/C_{60}/perovskite interface for the control, control + annealing , DAP and DAP + annealing devices. The images show similar values of PL peak wavelength with values of 734 nm for the control, and control + annealing, 733 nm for DAP and 732 nm for DAP + annealing device. The distributions of the PL peak wavelengths are shown as histograms in **Figure S12 e**. In **Figure 2 a-d** we show the PL peak wavelengths map of the Glass/ITO/SAM/perovskite interface of the same four devices. For both the control and DAP-treated devices the PL peak taken from the Glass/ITO/SAM interface is slightly more redshifted compared to the top with PL peak wavelengths of 742 nm for the control and 737 nm for the DAP-treated one. The blueshifted PL after DAP treatment can be rationalized with suppressed kinetics of photoinduced halide segregation and migration, which we previously reported for other amine-based surface

passivators.[51,52] Moreover, the blueshift could be related to the formation of additional lower dimensional polymorphs.[53] We have previously shown that for high additions of EDA in the precursor solution, we saw the formation of a 1D imidazolinium lead iodide secondary phase and a blue shifted cesium and bromide rich 3D, cubic, α-phase.[10] To verify this, we analyzed the crystal structure using X-ray diffraction (XRD) shown in **Figure S13**. The XRD patterns of the samples with excess DAP show no additional peaks from secondary phases. We also conducted Grazing Incidence Wide-Angle X-ray Scattering (GIWAXS) measurements to further study the surface and bulk film structures using different X-ray incidence angles. In **Figure S14** we show the GIWAXS patterns of the control samples and with addition of DAP 0.75, 10 and 75 mM. We see no detectable 2D or polytype structures emerge with the addition of excess DAP. From these structural findings we concluded that the observed photoluminescence blueshift in hyperspectral measurements after DAP passivation is most likely due to suppressed photoinduced halide segregation.

However, the redshift between top and bottom PL, shown comparing Figure S12e and Figure 2e, suggests that for both the control and DAP-treated device exhibit vertical heterogeneity in the perovskite layer. Specifically, the bottom interface (Glass/ITO/SAM) appears more iodide-rich, while the top interface (in contact with C60) shows a more uniform halide distribution. After annealing the back interface PL peak wavelength blueshifts, with an average PL peak at 736 nm for the control + annealing and 733 nm in the DAP + annealing (**Figure 2e**). This shift indicated that the perovskite layer after annealing has a more homogeneous wide bandgap composition throughout the device which might explain why the FF is improved only in this case potentially due to better electrical contact and/or energy alignment at both the top and bottom interlayers.

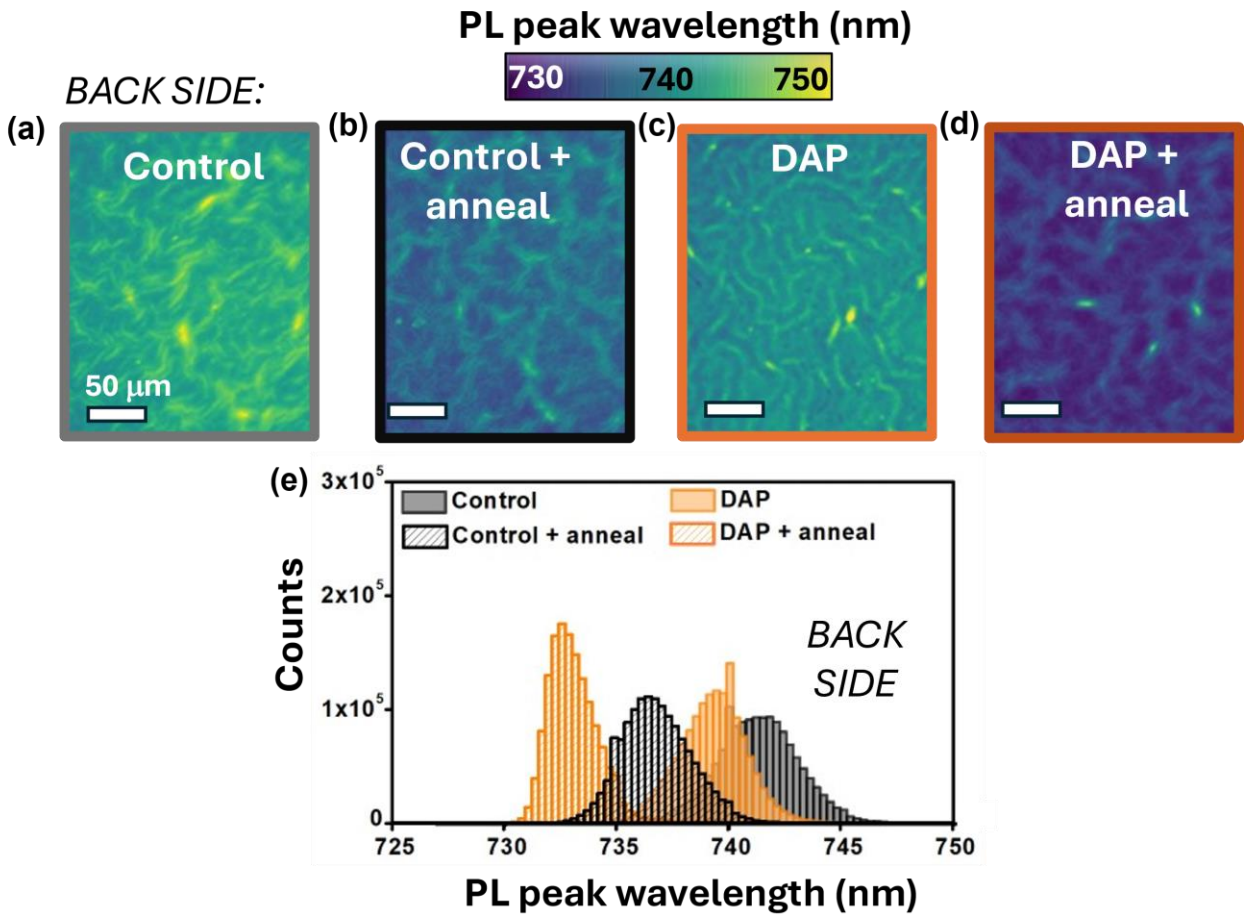

Figure 2*: a) PL peak wavelength map taken from the back ITO/SAM/perovskite interface of the control, b) control + annealing, c) DAP and d) DAP+ annealing solar cells. e) Histograms of the PL peak distribution from a-d.*

To better understand the chemistry behind DAP's effect on the surface, we performed time-of-flight secondary ion mass spectrometry (ToF-SIMS). We analyzed a set of three samples: one control sample, and two treated with DAP 0.75 mM and 10 mM solutions. DAP 0.75 mM is the concentration we found to be most effective for improving the efficiency of solar-cell devices, while we use 10 mM to observe possible trends in the formation of new molecular species. We have previously investigated the chemical reactivity of benzylamine (BA) and ethylenediamine (EDA) in solution with ^{1}H and ^{13}C-NMR spectroscopy and in films with ToF-SIMS when used as

an additive in the same $FA_{0.83}Cs_{0.17}Pb(I_{0.75}Br_{0.25})_3$ perovskite composition.[10,40] In those studies, we found that BA and EDA will react quickly and quantitatively with FA^+ in the perovskite precursor to form larger A-site cations which is subsequently incorporated into the thin film.

In **Figure 3a,** we illustrate a potential mechanism for the reaction of DAP with FA^+ at the film surface, in analogy to what we have observed previously with EDA-treatment.[10] The reaction between DAP and FA^+ would result in the formation of a six-membered ring in which the two nitrogen atoms of a FA^+ ion are linked by a propan-1,3-diyl bridge, i.e., 1,4,5,6-tetrahydropyrimidinium (THP^+), along with the elimination of two equivalents of volatile ammonia. In **Figure S15**, we describe this possible reaction mechanism in more detail. In **Figure 3b** we show the ToF-SIMS depth profiling results combined with 2D maps of FA^+ (m/z=45), THP^+ (m/z=85) and Si (m/z=28) mass fragments.[54] We observe an increase in the THP^+ signal at higher concentrations. This trend suggests that DAP is converted to THP^+ upon contact with FA^+ on the surface. Based on Figure 3b, we can see qualitatively that the THP^+ signal increases with higher DAP concentrations (10 mM), and it is present on the surface of both films after DAP 0.75 mM and 10 mM surface treatments. After converting the sputter time to film depth (assuming a total film thickness of 500 nm), we see that THP^+ is present in the first ~70 nm (**Figure S16**).

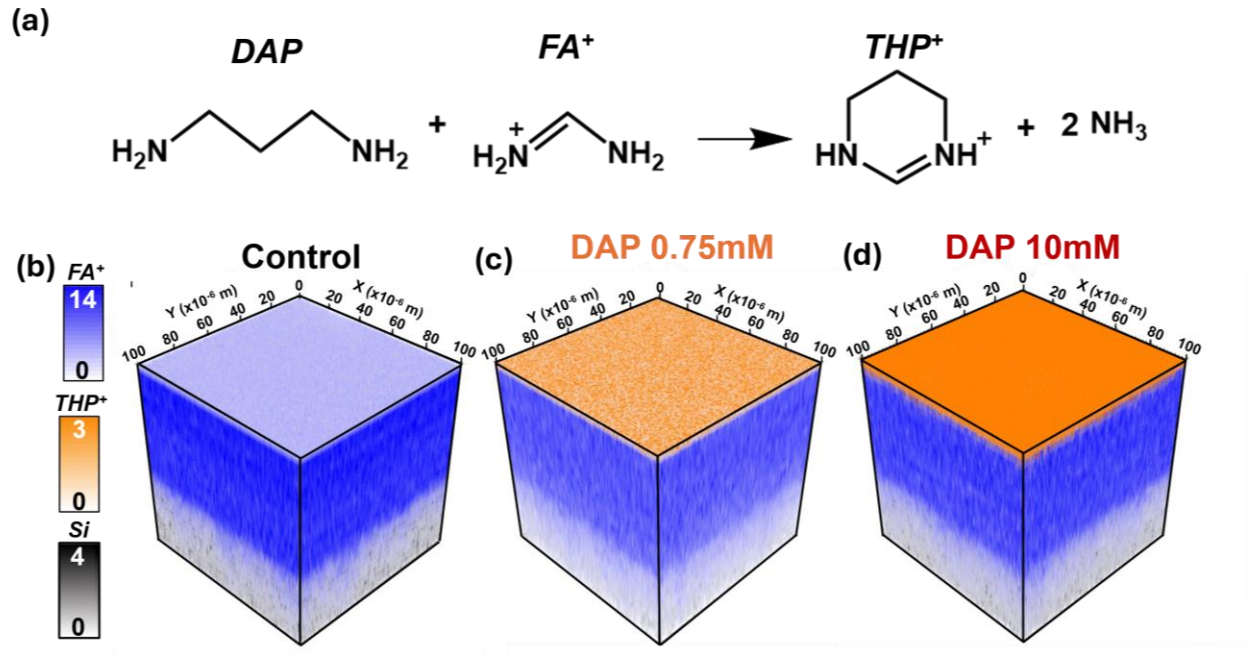

Figure 3: *a) Reaction scheme showing the 1,3-diaminopropane (DAP) surface passivator reacting with formamidinium (FA^+) cations present in the perovskite lattice to form 1,4,5,6-tetrahydropyrimidinium (THP^+) and ammonia (NH_3^+) stoichiometrically. b) ToF-SIMS depth profile of a control film, c) after surface treatment with DAP 0.75 mM and d) DAP 10 mM solution in IPA. The molecular fragment of FA^+ (CH_5N_2, m/z = 45.04) is shown in blue, THP^+ ($C_4H_9N_2$, m/z = 85.09) in orange and Si (m/z=27.97) in black.*

The improved compositional heterogeneity of the DAP + annealing devices suggest that this method would be suitable for achieving higher V_{OC} and FF in Si-perovskite tandem devices where the halide segregation of perovskite compositions of > 1.7 eV can be a limiting factor. We therefore made Si-perovskite tandems with different top layers: the control perovskite layer, DAP-treated perovskite, and perovskite that is DAP-treated and annealed post-processing. **Figure 4a** shows the overall device architecture. **Figure 4b** shows the J-V curve of our control Si-perovskite tandem and, in **Figure 4c** the one made with DAP passivation and annealing after C_{60} deposition for 1 min at 150 °C. **Figure S17** shows the Si-perovskite tandems J-V curves for devices made with DAP

only without annealing along with the average performance parameters in **Figure S18** and **Table S2**. We find that the V_{OC} progressively increases for the tandems containing DAP and DAP + annealing with a maximum of 1.915 V for the champion DAP + annealing tandem, 1.901 V for the champion control and 1.903 for the DAP. All the other solar-cell performance parameters maximize in the DAP + annealing with maximum FF of 0.70 (control= 0.65 and DAP = 0.63) and J_{SC} of 18.93 mA/cm^2 (control= 18.86 mA/cm^2, DAP = 18.79 mA/cm^2), resulting in PCE of 25.29% (Control = 23.26%, DAP = 22.72%).

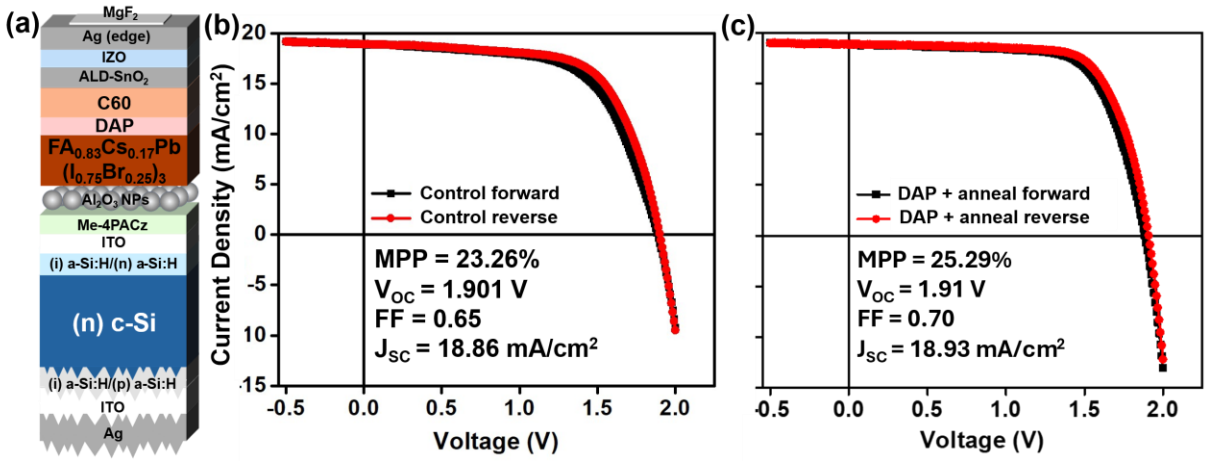

Figure 4*: a) Si-perovskite tandem architecture of devices made with the DAP surface passivation step. b) Current-voltage (J-V) curve of the control Si-perovskite tandem and c) DAP + annealing. The values were recorded from 1 cm^2 tandem devices shown in the Inset of the figure.*

Conclusion

We demonstrate the efficacy of combining surface treatment with a diamine molecule and incorporating a post-processing step of annealing the C_{60} interface to enhance the performance of 1.7 eV single-junction perovskite solar cells. Notably, we successfully implemented this approach successfully into a silicon-perovskite tandem device improving the PCE from 23.26% to 25.29% and achieving a champion cell FF of 0.70 and V_{OC} of 1.915 V. Moreover, we show that diamines

react with formamidinium (FA^+) cations when deposited on the perovskite surfaces, consistent with our previous work on solution-based reactions of primary amines with FA^+ cations. We note with interest the similarity between EDA, DAP, and the tail groups of the recently reported amine-silane based passivation schemes and posit that similar reactions may take place.[55] We speculate these reactions may relieve defects caused by FA^+ in interstitial spaces or antisites at the surface. We attribute the improvement in V_{OC} to the surface defect passivation effect of DAP and the improvement in FF to the post-annealing processing which enhances C_{60} adhesion and promotes a more uniform perovskite composition throughout the film depth. This research underscores the importance of developing a deeper chemical understanding of the chemical reactivity of diamines, which is essential for clarifying the mechanistic differences among various classes of molecular passivators. These results indicate that commonly simulated models of diamine coordination which involve bridging interactions between undercoordinated Pb^{2+} centers, need to be reexamined to ensure they accurately reflect the underlying chemistry.

Experimental Section

Single-junction devices:

Me-4PACz ([4-(3,6-dimethyl-9H-carbazol-9-yl)butyl]phosphonic acid) solution was prepared by dissolving it into DMF at a concentration of 50 mg/mL following procedure from Ref [56]. The concentrated Me-4PACz solution in DMF was then diluted to 1 mg/mL in IPA. Nanoparticle (np-) Al_2O_3 was prepared by adding 100 µl of Al_2O_3 nanoparticles(np) solution to 15 ml of anhydrous isopropyl alcohol to give a 1:150 vol ratio solution, which was stirred overnight before use. The perovskite $FA_{0.83}Cs_{0.17}Pb(I_{0.75}Br_{0.25})_3$ solution was prepared as a 5 mL 1.4 M stock containing 999.2 mg FAI, 309.2 mg CsI, 2016.9 mg PbI_2 and 963.4 mg $PbBr_2$ in 4:1 DMF:DMSO, which was stirred overnight. Before use, this solution was filtered with a 0.2 µm PTFE filter.

Pre-patterned indium tin oxide substrates were cleaned by scrubbing with 1% Decon90 solution, before sonicating sequentially in 1% Decon90, ionized water, acetone and isopropyl alcohol for ~10 minutes each, with rinsing between each step. Substrates were dried under N_2 and UV ozone treated for 30 minutes directly before use and transferred to an N_2 glovebox for fabrication with constant purging. Me-4PACz solution (150 µl) was spread over the substrate, and after 10 seconds spin coated at 3000 rpm for 30 s, before annealing at 100°C for 10 minutes. After cooling, we did an IPA washing step by spin-coating at the same speed 300 µl of IPA and annealed at 100 °C for 5 minutes. 70 µl of np-Al_2O_3 was dynamically spin-coated at 6000 rpm for 30 s, with ~ 1 min annealing at 100°C. The perovskite was spin coated at 1000 rpm (200 rpm/s ramp) for 10 s, followed by 45 s at 5000 rpm (1000 rpm/s ramp), with 170 µl of the solution dynamically coated 3 seconds into the program, and 330 µl of anisole was dropped as an antisolvent 10 s before the end of the program. The 1,3-diaminopropane (DAP) solution was prepared first by adding 2.5 mL to 3 mL of anhydrous IPA (10 mM). The 10 mM solution was then diluted to 0.75 mM by adding 150 mL of the 10 mM into 1.85 mL IPA. The 0.75 mM DAP solution was spin coated in a dry box of RH < 10% (in Oxford) or inside the N_2 glove box (University of Washington) at 4000 rpm (1000 rpm/s ramp) for 30 s and annealed at 100 °C for 10 minutes. 30nm C60 and 8 nm BCP layers are then evaporated under vacuum (~ $3x10^{-6}$ Torr). After evaporation of C60 and BCP the devices underscoring the post annealing step, were annealed at 150°C for one minute inside the glove box. The half-stacks were then re-introduced inside the thermal evaporator, to deposit 100 nm silver contacts at an initial rate of 0.2 Å/s (ramped up to 1 Å/s in 20 min) under high vacuum (~10^{-6} Torr).

Si-perovskite tandem devices:

Commercial M2 n-type Czochralski silicon wafers with resistivity of about 1 Ω.cm were used to prepare the tandem silicon bottom sub-cells based on the silicon heterojunction technology. To

obtain a differentiated surface morphology between the front and rear sides of the wafer, the silicon wafers underwent a two-step etching process: they were first polished in concentrated potassium hydroxide (KOH), thus simultaneously removing the saw-damaged zone at the wafer surface. After masking one side with silicon oxide, they underwent standard KOH texturing to obtain pyramid-like structures on the other side. After removal of the SiOx mask and cleaning, they were passivated with a final hydrofluoric acid dip. Similar preparation methods for differentiated front/rear surface morphology have been described elsewhere.[57,58] All the wet chemical etching and cleaning steps were performed in an industrial automatic wet bench from Akrion Solar. An intrinsic/n-type-doped (resp. intrinsic/p-type-doped) hydrogenated amorphous silicon (a-Si:H) stack was deposited on the chemically polished front side (resp. textured rear side) of the wafers by plasma-enhanced chemical vapor deposition (PECVD) in an industrial tool from Meyer Burger. Tin-doped indium oxide (ITO) layers were then deposited by magnetron pulsed DC sputtering in an industrial inline tool by Meyer Burger with a 97/3 wt.% In_2O_3/SnO_2 rotary target. A 70 nm-thick layer was deposited to ensure charge collection at the rear side of the tandem device, and a 12 nm-thick layer was deposited on the front side to form the carrier recombination layer at the interface between the top and bottom sub-cells of the tandem device. Metallic masks were used during the ITO deposition to define the active areas of the device. Finally, the M2 wafers were laser diced into 3 x 3 cm^2 substrates. The silicon substrates were pre-treated by annealing at 100 °C for 30 mins in air before UV ozone treated for 30 minutes. Then processing from the Me4-PACz till the C60 annealing step is the same for the single junction. A layer of SnO_2 was deposited instead of evaporating BCP through atomic layer deposition, followed by sputtering IZO and evaporating silver edge contact and MgF_2. Finally, 200 nm Ag was evaporated on the back side of the tandem device.

Characterization

Hyperspectral microscope:

Hyperspectral measurements were performed using a Photon etc. IMA upright microscope fitted with a transmitted darkfield condenser and a 20X objective (Nikon Plan Fluor, NA 0.45, CC 0-2). The excitation was done using a mercury halide lamp (Nikon ultrahigh pressure 130 W mercury lamp) passing through a 500 nm short-pass filter and emission was collected through a 500 dichroic filter and 550 nm long-pass filter. The lamp has six levels of light intensity, and all the measurements were taken using the highest (ND1) with total incident power on the sample of 1.63 W/cm^2. The Hyperspectral Microscope uses a tunable Bragg filter to image a sample at specific wavelengths. The sample is imaged throughout the spectral range and these images are combined into a single "Hyper Cube", which carries spectral information at each pixel. This allows for diffraction limited imaging, rather than being constrained by the spot size of the fiber optic cable. Post-processing was done in the proprietary Photon etc. PHySpec Software. The devices were encapsulated before the measurement using UV curable glue (Bluefixx) and microscope slides (VWR, 1 mm thick).

Time-of-Flight Secondary Ion Mass Spectrometry:

Positive ion ToF-SIMS depth profiles were acquired using an IONTOF TOF.SIMS 5 spectrometer. Profiles were acquired in the non-interlaced mode. Spectra/images were acquired using a pulsed 25 keV Bi^{3+} cluster ion source using high mass resolution mode. Data was acquired using a 100 μm x 100 μm spot at 256 x 256 pixels. The ion source was operated with a current of 0.02 pA to avoid saturation in the spectra. The primary ion dose per layer was 1.1×10^{11} ions/cm^2. Sputtering was done using a gas cluster ion source using 20 keV argon 1000 clusters with a current of 6.98 nA over an area of 500 μm x 500 μm. The sputter dose per layer was 5.1×10^{13} ions/cm^2. An electron flood gun and argon flooding were also used for charge neutralization. Positive ion data

were calibrated using the $C_2H_3^+$, Pb^+ and Cs_2I^+ peaks with calibration errors less than 40 ppm. Mass resolving power (m/Δm) for positive ion data was ~4500 for m/z = 27 ($C_2H_3^+$).

Grazing Incidence Wide-Angle X-ray Scattering:

GIWAXS measurements were conducted at the beamline 11-BM, Brookhaven National Laboratory. The samples were cut to an approximate size of 0.5 cm × 0.5 cm. Images were acquired at incidence angles of 0.05° and 0.5° to characterize surface and bulk structures respectively with an exposure time of 10 s, using an X-ray beam energy of 13.5 keV. Beam divergence was 1 mrad and energy resolution of 0.7%. Data analysis was performed on the SciAnalysis package provided by the beamline.

ASSOCIATED CONTENT

Supporting Information.

Additional methods, confocal and time resolved photoluminescence, GIWAXS and device characterization.

AUTHOR INFORMATION

Corresponding Author

David S. Ginger - Department of Chemistry, University of Washington, Seattle, WA 98195, USA, Physical Sciences Division, Physical and Computational Sciences Directorate, Pacific Northwest National Laboratory, Richland, Washington 99352, United States

Email: dginger@uw.edu

Authors

Margherita Taddei - Department of Chemistry, University of Washington, Seattle, WA 98195, USA

Hannah Contreras - Department of Chemistry, University of Washington, Seattle, WA 98195, USA

Hai-Nam Doan - Department of Physics, University of Oxford, Oxford, OX1 3PU, U.K., Institute of Materials Science, Technical University of Munich, München, 85748, Germany

Declan P. McCarthy - Department of Chemistry, University of Colorado-Boulder, Boulder, CO 80309, USA

Seongrok Seo - Department of Physics, University of Oxford, Oxford, OX1 3PU, U.K

Robert J. E. Westbrook - Department of Chemistry, University of Washington, Seattle, WA 98195, USA

Daniel J. Graham - Department of Bioengineering, University of Washington, Seattle, Washington 98195

Kunal Datta - School of Materials Science and Engineering, Georgia Institute of Technology, North Ave NW, Atlanta, Georgia 30332, USA

Perrine Carroy - Université Grenoble Alpes, CEA, Liten, Campus Ines, 73375 Le Bourget du Lac, France

Delfina Muñoz - Université Grenoble Alpes, CEA, Liten, Campus Ines, 73375 Le Bourget du Lac, France

Juan-Pablo Correa-Baena - School of Materials Science and Engineering, Georgia Institute of Technology, North Ave NW, Atlanta, Georgia 30332, USA

Stephen Barlow - Renewable and Sustainable Energy Institute, University of Colorado-Boulder, Boulder, CO 80309, USA

Seth R. Marder - Department of Chemistry, University of Colorado-Boulder, Boulder, CO 80309, USA, Renewable and Sustainable Energy Institute, University of Colorado-Boulder, Boulder, CO 80309, USA, Department of Chemical and Biological Engineering and Materials Science Program, University of Colorado-Boulder, Boulder, CO 80309, USA

Joel A. Smith - Department of Physics, University of Oxford, Oxford, OX1 3PU, U.K

Henry J. Snaith - Department of Physics, University of Oxford, Oxford, OX1 3PU, U.K

Author Contributions

M.T. and D.S.G. drafted the manuscript and conceived the idea. D.S.G., H.J.S, S.R.M, J.A.S., and S.B. supervised the project and directed the research. M.T., H.C., H.N.D., J.A.S. and R.J.E.W conducted experiments and analyzed the data. D.P.M. synthesized some of the molecules and helped with the interpretation of the chemical reaction. S.S. assisted with the fabrication of the Si-perovskite tandems. P.C. and D.M. provided the silicon substrates. K.D. and J.P.C.B. conducted and analyzed GIWAXS data. D.J.G. conducted the ToF-SIMS measurements. All authors contributed to the writing of the manuscript.

Notes

The authors declare the following competing financial interest(s): H.J.S. is a co-founder and CSO of Oxford PV Ltd.

Acknowledgments

This work was primarily funded by the Office of Naval Research (Award # N00014-20-1-2587). ToF-SIMS was carried out at the Molecular Analysis Facility, a National Nanotechnology Coordinated Infrastructure site at the University of Washington which is supported in part by the National Science Foundation (awards NNCI-2025489, NNCI-1542101), the Molecular Engineering & Sciences Institute, and the Clean Energy Institute. The CEA team acknowledges the NEXUS project funded from the European Union's Horizon Europe research and innovation program under grant agreement No. 101075330 for the fabrication of the Si bottom cell used in Si-perovskite tandem devices. Views and opinions expressed are, however, those of the author(s) only and do not necessarily reflect those of the European Union or RIA. Neither the European Union nor the granting authority can be held responsible for them. We thank the beamline scientists

Honghu Zhang and Ruipeng Li at the 11-BM CMS beamline at NSLS-II, Brookhaven National Lab.

References

(1) Hörantner, M. T.; Leijtens, T.; Ziffer, M. E.; Eperon, G. E.; Christoforo, M. G.; McGehee, M. D.; Snaith, H. J. The Potential of Multijunction Perovskite Solar Cells. *ACS Energy Lett.* **2017**, *2* (10), 2506–2513. https://doi.org/10.1021/acsenergylett.7b00647.

(2) Eperon, G. E.; Hörantner, M. T.; Snaith, H. J. Metal Halide Perovskite Tandem and Multiple-Junction Photovoltaics. *Nat Rev Chem* **2017**, *1* (12), 0095. https://doi.org/10.1038/s41570-017-0095.

(3) Eperon, G. E.; Leijtens, T.; Bush, K. A.; Prasanna, R.; Green, T.; Wang, J. T.-W.; McMeekin, D. P.; Volonakis, G.; Milot, R. L.; May, R.; Palmstrom, A.; Slotcavage, D. J.; Belisle, R. A.; Patel, J. B.; Parrott, E. S.; Sutton, R. J.; Ma, W.; Moghadam, F.; Conings, B.; Babayigit, A.; Boyen, H.-G.; Bent, S.; Giustino, F.; Herz, L. M.; Johnston, M. B.; McGehee, M. D.; Snaith, H. J. Perovskite-Perovskite Tandem Photovoltaics with Optimized Band Gaps. *Science* **2016**, *354* (6314), 861–865. https://doi.org/10.1126/science.aaf9717.

(4) Leijtens, T.; Bush, K. A.; Prasanna, R.; McGehee, M. D. Opportunities and Challenges for Tandem Solar Cells Using Metal Halide Perovskite Semiconductors. *Nat Energy* **2018**, *3* (10), 828–838. https://doi.org/10.1038/s41560-018-0190-4.

(5) McMeekin, D. P.; Sadoughi, G.; Rehman, W.; Eperon, G. E.; Saliba, M.; Horantner, M. T.; Haghighirad, A.; Sakai, N.; Korte, L.; Rech, B.; Johnston, M. B.; Herz, L. M.; Snaith, H. J. A Mixed-Cation Lead Mixed-Halide Perovskite Absorber for Tandem Solar Cells. *Science* **2016**, *351* (6269), 151–155. https://doi.org/10.1126/science.aad5845.

(6) *Best Research-Cell Efficiency Chart*. https://www.nrel.gov/pv/cell-efficiency.html (accessed 2024-04-13).

(7) Datta, K.; Laar, S. van; Taddei, M.; Hidalgo, J.; Kodalle, T.; Aalbers, G.; Lai, B.; Li, R.; Tamura, N.; Frencken, J.; Westbrook, R.; Graham, D.; Sutter-Fella, C.; Correa-Baena, J.-P.; Ginger, D.; Wienk, M.; Janssen, R. Local Halide Heterogeneity Drives Surface Wrinkling in Mixed-Halide Wide-Bandgap Perovskites. Research Square September 2, 2024. https://doi.org/10.21203/rs.3.rs-4814295/v1.

(8) Barker, A. J.; Sadhanala, A.; Deschler, F.; Gandini, M.; Senanayak, S. P.; Pearce, P. M.; Mosconi, E.; Pearson, A. J.; Wu, Y.; Srimath Kandada, A. R.; Leijtens, T.; De Angelis, F.; Dutton, S. E.; Petrozza, A.; Friend, R. H. Defect-Assisted Photoinduced Halide Segregation in Mixed-Halide Perovskite Thin Films. *ACS Energy Lett.* **2017**, *2* (6), 1416–1424. https://doi.org/10.1021/acsenergylett.7b00282.

(9) Motti, S. G.; Patel, J. B.; Oliver, R. D. J.; Snaith, H. J.; Johnston, M. B.; Herz, L. M. Phase Segregation in Mixed-Halide Perovskites Affects Charge-Carrier Dynamics While Preserving Mobility. *Nat Commun* **2021**, *12* (1), 6955. https://doi.org/10.1038/s41467-021-26930-4.

(10) Taddei, M.; Smith, J. A.; Gallant, B. M.; Zhou, S.; Westbrook, R. J. E.; Shi, Y.; Wang, J.; Drysdale, J. N.; McCarthy, D. P.; Barlow, S.; Marder, S. R.; Snaith, H. J.; Ginger, D. S. Ethylenediamine Addition Improves Performance and Suppresses Phase Instabilities in Mixed-Halide Perovskites. *ACS Energy Lett.* **2022**, 4265–4273. https://doi.org/10.1021/acsenergylett.2c01998.

(11) Unger, E. L.; Kegelmann, L.; Suchan, K.; Sörell, D.; Korte, L.; Albrecht, S. Roadmap and Roadblocks for the Band Gap Tunability of Metal Halide Perovskites. *J. Mater. Chem. A* **2017**, *5* (23), 11401–11409. https://doi.org/10.1039/C7TA00404D.

(12) Stolterfoht, M.; Caprioglio, P.; Wolff, C. M.; Márquez, J. A.; Nordmann, J.; Zhang, S.; Rothhardt, D.; Hörmann, U.; Amir, Y.; Redinger, A.; Kegelmann, L.; Zu, F.; Albrecht, S.; Koch, N.; Kirchartz, T.; Saliba, M.; Unold, T.; Neher, D. The Impact of Energy Alignment and Interfacial Recombination on the Internal and External Open-Circuit Voltage of Perovskite Solar Cells. *Energy Environ. Sci.* **2019**, *12* (9), 2778–2788. https://doi.org/10.1039/C9EE02020A.

(13) Caprioglio, P.; Smith, J. A.; Oliver, R. D. J.; Dasgupta, A.; Choudhary, S.; Farrar, M. D.; Ramadan, A. J.; Lin, Y.-H.; Christoforo, M. G.; Ball, J. M.; Diekmann, J.; Thiesbrummel, J.; Zaininger, K.-A.; Shen, X.; Johnston, M. B.; Neher, D.; Stolterfoht, M.; Snaith, H. J. Open-Circuit and Short-Circuit Loss Management in Wide-Gap Perovskite p-i-n Solar Cells. *Nat Commun* **2023**, *14* (1), 932. https://doi.org/10.1038/s41467-023-36141-8.

(14) Correa-Baena, J.-P.; Tress, W.; Domanski, K.; Anaraki, E. H.; Turren-Cruz, S.-H.; Roose, B.; Boix, P. P.; Grätzel, M.; Saliba, M.; Abate, A.; Hagfeldt, A. Identifying and Suppressing Interfacial Recombination to Achieve High Open-Circuit Voltage in Perovskite Solar Cells. *Energy Environ. Sci.* **2017**, *10* (5), 1207–1212. https://doi.org/10.1039/C7EE00421D.

(15) Tong, J.; Jiang, Q.; Zhang, F.; Kang, S. B.; Kim, D. H.; Zhu, K. Wide-Bandgap Metal Halide Perovskites for Tandem Solar Cells. *ACS Energy Lett.* **2021**, *6* (1), 232–248. https://doi.org/10.1021/acsenergylett.0c02105.

(16) Lee, J. E.; Motti, S. G.; Oliver, R. D. J.; Yan, S.; Snaith, H. J.; Johnston, M. B.; Herz, L. M. Unraveling Loss Mechanisms Arising from Energy-Level Misalignment between Metal Halide Perovskites and Hole Transport Layers. *Advanced Functional Materials* **2024**, *34* (30), 2401052. https://doi.org/10.1002/adfm.202401052.

(17) Wojciechowski, K.; Leijtens, T.; Siprova, S.; Schlueter, C.; Hörantner, M. T.; Wang, J. T.-W.; Li, C.-Z.; Jen, A. K.-Y.; Lee, T.-L.; Snaith, H. J. C60 as an Efficient N-Type Compact Layer in Perovskite Solar Cells. *J. Phys. Chem. Lett.* **2015**, *6* (12), 2399–2405. https://doi.org/10.1021/acs.jpclett.5b00902.

(18) Warby, J.; Zu, F.; Zeiske, S.; Gutierrez-Partida, E.; Frohloff, L.; Kahmann, S.; Frohna, K.; Mosconi, E.; Radicchi, E.; Lang, F.; Shah, S.; Peña-Camargo, F.; Hempel, H.; Unold, T.; Koch, N.; Armin, A.; De Angelis, F.; Stranks, S. D.; Neher, D.; Stolterfoht, M. Understanding Performance Limiting Interfacial Recombination in Pin Perovskite Solar Cells. *Advanced Energy Materials* **2022**, *12* (12), 2103567. https://doi.org/10.1002/aenm.202103567.

(19) Oliver, R. D. J.; Caprioglio, P.; Peña-Camargo, F.; Buizza, L. R. V.; Zu, F.; Ramadan, A. J.; Motti, S. G.; Mahesh, S.; McCarthy, M. M.; Warby, J. H.; Lin, Y.-H.; Koch, N.; Albrecht, S.; Herz, L. M.; Johnston, M. B.; Neher, D.; Stolterfoht, M.; Snaith, H. J. Understanding and Suppressing Non-Radiative Losses in Methylammonium-Free Wide-Bandgap Perovskite Solar Cells. *Energy Environ. Sci.* **2022**, *15* (2), 714–726. https://doi.org/10.1039/D1EE02650J.

(20) Ye, F.; Zhang, S.; Warby, J.; Wu, J.; Gutierrez-Partida, E.; Lang, F.; Shah, S.; Saglamkaya, E.; Sun, B.; Zu, F.; Shoaee, S.; Wang, H.; Stiller, B.; Neher, D.; Zhu, W.-H.; Stolterfoht, M.; Wu, Y. Overcoming C60-Induced Interfacial Recombination in Inverted Perovskite Solar Cells by Electron-Transporting Carborane. *Nat Commun* **2022**, *13* (1), 7454. https://doi.org/10.1038/s41467-022-34203-x.

(21) Stolterfoht, M.; Wolff, C. M.; Márquez, J. A.; Zhang, S.; Hages, C. J.; Rothhardt, D.; Albrecht, S.; Burn, P. L.; Meredith, P.; Unold, T.; Neher, D. Visualization and Suppression of Interfacial Recombination for High-Efficiency Large-Area Pin Perovskite Solar Cells. *Nat Energy* **2018**, *3* (10), 847–854. https://doi.org/10.1038/s41560-018-0219-8.

(22) Chen, B.; Yang, M.; Priya, S.; Zhu, K. Origin of J–V Hysteresis in Perovskite Solar Cells. *J. Phys. Chem. Lett.* **2016**, *7* (5), 905–917. https://doi.org/10.1021/acs.jpclett.6b00215.
(23) Shao, Y.; Xiao, Z.; Bi, C.; Yuan, Y.; Huang, J. Origin and Elimination of Photocurrent Hysteresis by Fullerene Passivation in CH3NH3PbI3 Planar Heterojunction Solar Cells. *Nat Commun* **2014**, *5* (1), 5784. https://doi.org/10.1038/ncomms6784.
(24) Anselmo, A. S.; Dzwilewski, A.; Svensson, K.; Moons, E. Photodegradation of the Electronic Structure of PCBM and C60 Films in Air. *Chemical Physics Letters* **2016**, *652*, 220–224. https://doi.org/10.1016/j.cplett.2016.04.003.
(25) Luo, D.; Su, R.; Zhang, W.; Gong, Q.; Zhu, R. Minimizing Non-Radiative Recombination Losses in Perovskite Solar Cells. *Nat Rev Mater* **2020**, *5* (1), 44–60. https://doi.org/10.1038/s41578-019-0151-y.
(26) Wang, J.; Fu, W.; Jariwala, S.; Sinha, I.; Jen, A. K.-Y.; Ginger, D. S. Reducing Surface Recombination Velocities at the Electrical Contacts Will Improve Perovskite Photovoltaics. *ACS Energy Lett.* **2019**, *4* (1), 222–227. https://doi.org/10.1021/acsenergylett.8b02058.
(27) Westbrook, R. J. E.; Macdonald, T. J.; Xu, W.; Lanzetta, L.; Marin-Beloqui, J. M.; Clarke, T. M.; Haque, S. A. Lewis Base Passivation Mediates Charge Transfer at Perovskite Heterojunctions. *J. Am. Chem. Soc.* **2021**, *143* (31), 12230–12243. https://doi.org/10.1021/jacs.1c05122.
(28) deQuilettes, D. W.; Koch, S.; Burke, S.; Paranji, R. K.; Shropshire, A. J.; Ziffer, M. E.; Ginger, D. S. Photoluminescence Lifetimes Exceeding 8 Ms and Quantum Yields Exceeding 30% in Hybrid Perovskite Thin Films by Ligand Passivation. *ACS Energy Lett.* **2016**, *1* (2), 438–444. https://doi.org/10.1021/acsenergylett.6b00236.
(29) Jariwala, S.; Burke, S.; Dunfield, S.; Shallcross, R. C.; Taddei, M.; Wang, J.; Eperon, G. E.; Armstrong, N. R.; Berry, J. J.; Ginger, D. S. Reducing Surface Recombination Velocity of Methylammonium-Free Mixed-Cation Mixed-Halide Perovskites via Surface Passivation. *Chem. Mater.* **2021**, *33* (13), 5035–5044. https://doi.org/10.1021/acs.chemmater.1c00848.
(30) Ansari, F.; Shirzadi, E.; Salavati-Niasari, M.; LaGrange, T.; Nonomura, K.; Yum, J.-H.; Sivula, K.; Zakeeruddin, S. M.; Nazeeruddin, M. K.; Grätzel, M.; Dyson, P. J.; Hagfeldt, A. Passivation Mechanism Exploiting Surface Dipoles Affords High-Performance Perovskite Solar Cells. *J. Am. Chem. Soc.* **2020**, *142* (26), 11428–11433. https://doi.org/10.1021/jacs.0c01704.
(31) Liu, C.; Yang, Y.; Chen, H.; Xu, J.; Liu, A.; Bati, A. S. R.; Zhu, H.; Grater, L.; Hadke, S. S.; Huang, C.; Sangwan, V. K.; Cai, T.; Shin, D.; Chen, L. X.; Hersam, M. C.; Mirkin, C. A.; Chen, B.; Kanatzidis, M. G.; Sargent, E. H. Bimolecularly Passivated Interface Enables Efficient and Stable Inverted Perovskite Solar Cells. *Science* **2023**, *382* (6672), 810–815. https://doi.org/10.1126/science.adk1633.
(32) Wu, W.-Q.; Yang, Z.; Rudd, P. N.; Shao, Y.; Dai, X.; Wei, H.; Zhao, J.; Fang, Y.; Wang, Q.; Liu, Y.; Deng, Y.; Xiao, X.; Feng, Y.; Huang, J. Bilateral Alkylamine for Suppressing Charge Recombination and Improving Stability in Blade-Coated Perovskite Solar Cells. *Science Advances* **2019**, *5* (3), eaav8925. https://doi.org/10.1126/sciadv.aav8925.
(33) Li, C.; Chen, L.; Jiang, F.; Song, Z.; Wang, X.; Balvanz, A.; Ugur, E.; Liu, Y.; Liu, C.; Maxwell, A.; Chen, H.; Liu, Y.; Wang, Z.; Xia, P.; Li, Y.; Fu, S.; Sun, N.; Grice, C. R.; Wu, X.; Fink, Z.; Hu, Q.; Zeng, L.; Jung, E.; Wang, J.; Park, S. M.; Luo, D.; Chen, C.; Shen, J.; Han, Y.; Perini, C. A. R.; Correa-Baena, J.-P.; Lu, Z.-H.; Russell, T. P.; De Wolf, S.; Kanatzidis, M. G.; Ginger, D. S.; Chen, B.; Yan, Y.; Sargent, E. H. Diamine Chelates for Increased Stability in Mixed Sn–Pb and All-Perovskite Tandem Solar Cells. *Nat Energy* **2024**, 1–9. https://doi.org/10.1038/s41560-024-01613-8.

(34) Hu, S.; Otsuka, K.; Murdey, R.; Nakamura, T.; Truong, M. A.; Yamada, T.; Handa, T.; Matsuda, K.; Nakano, K.; Sato, A.; Marumoto, K.; Tajima, K.; Kanemitsu, Y.; Wakamiya, A. Optimized Carrier Extraction at Interfaces for 23.6% Efficient Tin–Lead Perovskite Solar Cells. *Energy Environ. Sci.* **2022**, *15* (5), 2096–2107. https://doi.org/10.1039/D2EE00288D.
(35) Alharbi, E. A.; Alyamani, A. Y.; Kubicki, D. J.; Uhl, A. R.; Walder, B. J.; Alanazi, A. Q.; Luo, J.; Burgos-Caminal, A.; Albadri, A.; Albrithen, H.; Alotaibi, M. H.; Moser, J.-E.; Zakeeruddin, S. M.; Giordano, F.; Emsley, L.; Grätzel, M. Atomic-Level Passivation Mechanism of Ammonium Salts Enabling Highly Efficient Perovskite Solar Cells. *Nat Commun* **2019**, *10* (1), 3008. https://doi.org/10.1038/s41467-019-10985-5.
(36) Yang, Y.; Chen, H.; Liu, C.; Xu, J.; Huang, C.; Malliakas, C. D.; Wan, H.; Bati, A. S. R.; Wang, Z.; Reynolds, R. P.; Gilley, I. W.; Kitade, S.; Wiggins, T. E.; Zeiske, S.; Suragtkhuu, S.; Batmunkh, M.; Chen, L. X.; Chen, B.; Kanatzidis, M. G.; Sargent, E. H. Amidination of Ligands for Chemical and Field-Effect Passivation Stabilizes Perovskite Solar Cells. *Science* **2024**, *386* (6724), 898–902. https://doi.org/10.1126/science.adr2091.
(37) Liu, C.; Yang, Y.; Chen, H.; Xu, J.; Liu, A.; Bati, A. S. R.; Zhu, H.; Grater, L.; Hadke, S. S.; Huang, C.; Sangwan, V. K.; Cai, T.; Shin, D.; Chen, L. X.; Hersam, M. C.; Mirkin, C. A.; Chen, B.; Kanatzidis, M. G.; Sargent, E. H. Bimolecularly Passivated Interface Enables Efficient and Stable Inverted Perovskite Solar Cells. *Science* **2023**, *382* (6672), 810–815. https://doi.org/10.1126/science.adk1633.
(38) Chen, H.; Maxwell, A.; Li, C.; Teale, S.; Chen, B.; Zhu, T.; Ugur, E.; Harrison, G.; Grater, L.; Wang, J.; Wang, Z.; Zeng, L.; Park, S. M.; Chen, L.; Serles, P.; Awni, R. A.; Subedi, B.; Zheng, X.; Xiao, C.; Podraza, N. J.; Filleter, T.; Liu, C.; Yang, Y.; Luther, J. M.; De Wolf, S.; Kanatzidis, M. G.; Yan, Y.; Sargent, E. H. Regulating Surface Potential Maximizes Voltage in All-Perovskite Tandems. *Nature* **2023**, *613* (7945), 676–681. https://doi.org/10.1038/s41586-022-05541-z.
(39) Feng, W.; Tan, Y.; Yang, M.; Jiang, Y.; Lei, B.-X.; Wang, L.; Wu, W.-Q. Small Amines Bring Big Benefits to Perovskite-Based Solar Cells and Light-Emitting Diodes. *Chem* **2022**, *8* (2), 351–383. https://doi.org/10.1016/j.chempr.2021.11.010.
(40) Zhou, S.; Gallant, B. M.; Zhang, J.; Shi, Y.; Smith, J.; Drysdale, J. N.; Therdkatanyuphong, P.; Taddei, M.; McCarthy, D. P.; Barlow, S.; Kilbride, R. C.; Dasgupta, A.; Marshall, A. R.; Wang, J.; Kubicki, D. J.; Ginger, D. S.; Marder, S. R.; Snaith, H. J. Reactive Passivation of Wide-Bandgap Organic–Inorganic Perovskites with Benzylamine. *J. Am. Chem. Soc.* **2024**, *146* (40), 27405–27416. https://doi.org/10.1021/jacs.4c06659.
(41) Jin, H.; Farrar, M. D.; Ball, J. M.; Dasgupta, A.; Caprioglio, P.; Narayanan, S.; Oliver, R. D. J.; Rombach, F. M.; Putland, B. W. J.; Johnston, M. B.; Snaith, H. J. Alumina Nanoparticle Interfacial Buffer Layer for Low-Bandgap Lead-Tin Perovskite Solar Cells. *Advanced Functional Materials* **2023**, *33* (35), 2303012. https://doi.org/10.1002/adfm.202303012.
(42) Song, S.; Hill, R.; Choi, K.; Wojciechowski, K.; Barlow, S.; Leisen, J.; Snaith, H. J.; Marder, S. R.; Park, T. Surface Modified Fullerene Electron Transport Layers for Stable and Reproducible Flexible Perovskite Solar Cells. *Nano Energy* **2018**, *49*, 324–332. https://doi.org/10.1016/j.nanoen.2018.04.068.
(43) Khenkin, M. V.; Katz, E. A.; Abate, A.; Bardizza, G.; Berry, J. J.; Brabec, C.; Brunetti, F.; Bulović, V.; Burlingame, Q.; Di Carlo, A.; Cheacharoen, R.; Cheng, Y.-B.; Colsmann, A.; Cros, S.; Domanski, K.; Dusza, M.; Fell, C. J.; Forrest, S. R.; Galagan, Y.; Di Girolamo, D.; Grätzel, M.; Hagfeldt, A.; von Hauff, E.; Hoppe, H.; Kettle, J.; Köbler, H.; Leite, M. S.; Liu, S. (Frank); Loo, Y.-L.; Luther, J. M.; Ma, C.-Q.; Madsen, M.; Manceau, M.; Matheron, M.; McGehee, M.; Meitzner, R.; Nazeeruddin, M. K.; Nogueira, A. F.; Odabaşı, Ç.;

Osherov, A.; Park, N.-G.; Reese, M. O.; De Rossi, F.; Saliba, M.; Schubert, U. S.; Snaith, H. J.; Stranks, S. D.; Tress, W.; Troshin, P. A.; Turkovic, V.; Veenstra, S.; Visoly-Fisher, I.; Walsh, A.; Watson, T.; Xie, H.; Yıldırım, R.; Zakeeruddin, S. M.; Zhu, K.; Lira-Cantu, M. Consensus Statement for Stability Assessment and Reporting for Perovskite Photovoltaics Based on ISOS Procedures. *Nat Energy* **2020**, *5* (1), 35–49. https://doi.org/10.1038/s41560-019-0529-5.

(44) Frohna, K.; Anaya, M.; Macpherson, S.; Sung, J.; Doherty, T. A. S.; Chiang, Y.-H.; Winchester, A. J.; Orr, K. W. P.; Parker, J. E.; Quinn, P. D.; Dani, K. M.; Rao, A.; Stranks, S. D. Nanoscale Chemical Heterogeneity Dominates the Optoelectronic Response of Alloyed Perovskite Solar Cells. *Nat. Nanotechnol.* **2022**, *17* (2), 190–196. https://doi.org/10.1038/s41565-021-01019-7.

(45) Westbrook, R. J. E.; Taddei, M.; Giridharagopal, R.; Jiang, M.; Gallagher, S. M.; Guye, K. N.; Warga, A. I.; Haque, S. A.; Ginger, D. S. Local Background Hole Density Drives Nonradiative Recombination in Tin Halide Perovskites. *ACS Energy Lett.* **2024**, *9* (2), 732–739. https://doi.org/10.1021/acsenergylett.3c02701.

(46) Perini, C. A. R.; Castro-Mendez, A.-F.; Kodalle, T.; Ravello, M.; Hidalgo, J.; Gomez-Dominguez, M.; Li, R.; Taddei, M.; Giridharagopal, R.; Pothoof, J.; Sutter-Fella, C. M.; Ginger, D. S.; Correa-Baena, J.-P. Vapor-Deposited $n = 2$ Ruddlesden–Popper Interface Layers Aid Charge Carrier Extraction in Perovskite Solar Cells. *ACS Energy Lett.* **2023**, 1408–1415. https://doi.org/10.1021/acsenergylett.2c02419.

(47) Huang, Z.; Jiang, F.; Song, Z.; Dolia, K.; Zhu, T.; Yan, Y.; Ginger, D. S. Local A-Site Phase Segregation Leads to Cs-Rich Regions Showing Accelerated Photodegradation in Mixed-Cation Perovskite Semiconductor Films. *ACS Energy Lett.* **2024**, 3066–3073. https://doi.org/10.1021/acsenergylett.4c00960.

(48) Taddei, M.; Jariwala, S.; Westbrook, R. J. E.; Gallagher, S.; Weaver, A. C.; Pothoof, J.; Ziffer, M. E.; Snaith, H. J.; Ginger, D. S. Interpreting Halide Perovskite Semiconductor Photoluminescence Kinetics. *ACS Energy Lett.* **2024**, 2508–2516. https://doi.org/10.1021/acsenergylett.4c00614.

(49) Braunger, S.; Mundt, L. E.; Wolff, C. M.; Mews, M.; Rehermann, C.; Jošt, M.; Tejada, A.; Eisenhauer, D.; Becker, C.; Guerra, J. A.; Unger, E.; Korte, L.; Neher, D.; Schubert, M. C.; Rech, B.; Albrecht, S. $Cs_x FA_{1-x} Pb(I_{1-y} Br_y)_3$ Perovskite Compositions: The Appearance of Wrinkled Morphology and Its Impact on Solar Cell Performance. *J. Phys. Chem. C* **2018**, *122* (30), 17123–17135. https://doi.org/10.1021/acs.jpcc.8b06459.

(50) Kim, S.-G.; Kim, J.-H.; Ramming, P.; Zhong, Y.; Schötz, K.; Kwon, S. J.; Huettner, S.; Panzer, F.; Park, N.-G. How Antisolvent Miscibility Affects Perovskite Film Wrinkling and Photovoltaic Properties. *Nat Commun* **2021**, *12* (1), 1554. https://doi.org/10.1038/s41467-021-21803-2.

(51) Pothoof, J.; Westbrook, R. J. E.; Giridharagopal, R.; Breshears, M. D.; Ginger, D. S. Surface Passivation Suppresses Local Ion Motion in Halide Perovskites. *J. Phys. Chem. Lett.* **2023**, *14* (26), 6092–6098. https://doi.org/10.1021/acs.jpclett.3c01089.

(52) Akrami, F.; Jiang, F.; Giridharagopal, R.; Ginger, D. S. Kinetic Suppression of Photoinduced Halide Migration in Wide Bandgap Perovskites via Surface Passivation. *J. Phys. Chem. Lett.* **2023**, *14* (41), 9310–9315. https://doi.org/10.1021/acs.jpclett.3c02570.

(53) Guo, R.; Buyruk, A.; Jiang, X.; Chen, W.; Reb, L. K.; Scheel, M. A.; Ameri, T.; Müller-Buschbaum, P. Tailoring the Orientation of Perovskite Crystals via Adding Two-Dimensional Polymorphs for Perovskite Solar Cells. *J. Phys. Energy* **2020**, *2* (3), 034005. https://doi.org/10.1088/2515-7655/ab90d0.

(54) Taddei, M.; Graham, D. J. Mixed-Cation, Mixed-Halide Perovskite ToF-SIMS Spectra. *Surface Science Spectra* **2024**, *31* (1), 015004. https://doi.org/10.1116/6.0003624.
(55) Lin, Y.-H.; null, V.; Yang, F.; Cao, X.-L.; Dasgupta, A.; Oliver, R. D. J.; Ulatowski, A. M.; McCarthy, M. M.; Shen, X.; Yuan, Q.; Christoforo, M. G.; Yeung, F. S. Y.; Johnston, M. B.; Noel, N. K.; Herz, L. M.; Islam, M. S.; Snaith, H. J. Bandgap-Universal Passivation Enables Stable Perovskite Solar Cells with Low Photovoltage Loss. *Science* **2024**, *384* (6697), 767–775. https://doi.org/10.1126/science.ado2302.
(56) Liu, M.; Bi, L.; Jiang, W.; Zeng, Z.; Tsang, S.-W.; Lin, F. R.; Jen, A. K.-Y. Compact Hole-Selective Self-Assembled Monolayers Enabled by Disassembling Micelles in Solution for Efficient Perovskite Solar Cells. *Advanced Materials* **2023**, *35* (46), 2304415. https://doi.org/10.1002/adma.202304415.
(57) Al-Ashouri, A.; Köhnen, E.; Li, B.; Magomedov, A.; Hempel, H.; Caprioglio, P.; Márquez, J. A.; Morales Vilches, A. B.; Kasparavicius, E.; Smith, J. A.; Phung, N.; Menzel, D.; Grischek, M.; Kegelmann, L.; Skroblin, D.; Gollwitzer, C.; Malinauskas, T.; Jošt, M.; Matič, G.; Rech, B.; Schlatmann, R.; Topič, M.; Korte, L.; Abate, A.; Stannowski, B.; Neher, D.; Stolterfoht, M.; Unold, T.; Getautis, V.; Albrecht, S. Monolithic Perovskite/Silicon Tandem Solar Cell with >29% Efficiency by Enhanced Hole Extraction. *Science* **2020**, *370* (6522), 1300–1309. https://doi.org/10.1126/science.abd4016.
(58) Köhnen, E.; Wagner, P.; Lang, F.; Cruz, A.; Li, B.; Roß, M.; Jošt, M.; Morales-Vilches, A. B.; Topič, M.; Stolterfoht, M.; Neher, D.; Korte, L.; Rech, B.; Schlatmann, R.; Stannowski, B.; Albrecht, S. 27.9% Efficient Monolithic Perovskite/Silicon Tandem Solar Cells on Industry Compatible Bottom Cells. *Solar RRL* **2021**, *5* (7), 2100244. https://doi.org/10.1002/solr.202100244.